Astronomy & Astrophysics manuscript no. May 16, 2006
(DOI: will be inserted by hand later)

Accurate photometric redshifts for the CFHT Legacy Survey calibrated using the VIMOS VLT Deep Survey ⋆

O. Ilbert[1,2], S. Arnouts[2], H.J. McCracken[3,4], M. Bolzonella[1], E. Bertin[3,4], O. Le Fèvre[2], Y. Mellier[3,4], G. Zamorani[5], R. Pellò[6], A. Iovino[7], L. Tresse[2], D. Bottini[8], B. Garilli[8], V. Le Brun[2], D. Maccagni[8], J.P. Picat[6], R. Scaramella[9], M. Scodeggio[8], G. Vettolani[10], A. Zanichelli[10], C. Adami[2], S. Bardelli[5], A. Cappi[5], S. Charlot[11,3], P. Ciliegi[5], T. Contini[6], O. Cucciati[7], S. Foucaud[8], P. Franzetti[8], I. Gavignaud[11], L. Guzzo[8], B. Marano[1], C. Marinoni[2,12], A. Mazure[2], B. Meneux[2], R. Merighi[5], S. Paltani[13,14], A. Pollo[2], L. Pozzetti[5], M. Radovich[15], E. Zucca[5], M. Bondi[10], A. Bongiorno[1], G. Busarello[15], S. De La Torre[2], L. Gregorini[7], F. Lamareille[6], G. Mathez[6], P. Merluzzi[15], V. Ripepi[15], D. Rizzo[6], and D. Vergani[8]

[1] Università di Bologna, Dipartimento di Astronomia - Via Ranzani 1, 40127, Bologna, Italy
[2] Laboratoire d'Astrophysique de Marseille, UMR 6110 CNRS-Université de Provence, BP8, 13376 Marseille Cedex 12, France
[3] Institut d'Astrophysique de Paris, UMR7095 CNRS, Université Pierre & Marie Curie, 98 bis boulevard Arago, 75014 Paris, France
[4] Observatoire de Paris, LERMA, 61 Avenue de l'Observatoire, 75014 Paris, France
[5] INAF-Osservatorio Astronomico di Bologna - Via Ranzani 1, 40127, Bologna, Italy
[6] Laboratoire d'Astrophysique de l'Observatoire Midi-Pyrénées, UMR 5572, 14 avenue E. Belin, 31400 Toulouse, France
[7] INAF-Osservatorio Astronomico di Brera - Via Brera 28, Milan, Italy
[8] IASF-INAF - via Bassini 15, 20133, Milano, Italy
[9] INAF-Osservatorio Astronomico di Roma - Via di Frascati 33, 00040, Monte Porzio Catone, Italy
[10] IRA-INAF - Via Gobetti,101, 40129, Bologna, Italy
[11] European Southern Observatory, Garching, Germany
[12] Centre de Physique Théorique, Marseille, France
[13] Integral Science Data Centre, ch. d'Écogia 16, CH-1290 Versoix
[14] Geneva Observatory, ch. des Maillettes 51, CH-1290 Sauverny
[15] INAF-Osservatorio Astronomico di Capodimonte - Via Moiariello 16, 80131, Napoli, Italy

Received ... / Accepted ...

Abstract. We present and release photometric redshifts for an uniquely large and deep sample of 522286 objects with $i'_{AB} \leq 25$ in the Canada-France Legacy Survey "Deep Survey" fields D1, D2, D3, and D4, which cover a total effective area of 3.2 deg^2. We use 3241 spectroscopic redshifts with $0 \leq z \leq 5$ from the VIMOS VLT Deep Survey as a calibration and training set to derive these photometric redshifts. Using the "Le Phare" photometric redshift code, we devise a robust calibration method based on an iterative zero-point refinement combined with a template optimisation procedure and the application of a Bayesian approach. This method removes systematic trends in the photometric redshifts and significantly reduces the fraction of catastrophic errors (by a factor of 2.3), a significant improvement over traditional methods. We use our unique spectroscopic sample to present a detailed assessment of the robustness of the photometric redshift sample. For a sample selected at $i'_{AB} \leq 24$, we reach a redshift accuracy of $\sigma_{\Delta z/(1+z)} = 0.037$ with $\eta = 3.7\%$ of catastrophic errors (defined strictly as those objects with $\Delta z/(1+z) > 0.15$). The reliability of our photometric redshifts is lower for fainter objects: we find $\sigma_{\Delta z/(1+z)} = 0.029, 0.043$ and $\eta = 1.7\%, 5.4\%$ for samples selected at $i'_{AB} = 17.5 - 22.5$ and $22.5 - 24$ respectively. We find that the photometric redshifts of starburst galaxies in our sample are less reliable: although these galaxies represent only 18% of the spectroscopic sample they are responsible for 54% of the catastrophic errors. An analysis as a function of redshift demonstrates that our photometric redshifts work best in the redshift range $0.2 \leq z \leq 1.5$. We find an excellent agreement between the photometric and the VIMOS-VLT deep survey (VVDS) spectroscopic redshift distributions at $i'_{AB} \leq 24$ for the CFHTLS-D1 field. Finally, we compare the redshift distributions of i' selected galaxies on the four CFHTLS deep fields, showing that cosmic variance is already present on fields of $0.7 - 0.9$ deg^2. These photometric redshifts will be made publicly available from 1st may 2006 at *http://terapix.iap.fr* and *http://cencosw.oamp.fr/*.

Key words. Galaxies: distances and redshifts - Galaxies: photometry - Methods: data analysis

1. Introduction

A key factor in the study of galaxy evolution has been our ability to acquire large, deep, well-defined redshift samples covering substantial volumes of the Universe. Since the photometric redshift measurement relies only on the measurement of observed colours (Baum 1962), this technique can be an efficient way to assemble large and faint samples of galaxies extending to high redshift. Moreover, the photometric redshift method is also the only way to estimate redshifts beyond the spectroscopic limit (Sawicki et al. 1997, Arnouts et al. 1999, Benítez 2000, Fontana et al. 2000, Bolzonella et al. 2002).

However, this greatly increased redshift-gathering capability comes at at price, namely their much lower accuracy with respect to spectroscopic measurements. The most accurate photometric redshifts with medium band filters (Wolf et al. 2004) still remains around thirty times less accurate than redshifts measured with low resolution spectroscopy (Le Fèvre et al. 2004b). Despite this, for many studies of the galaxy population, such the galaxy luminosity function, the velocity accuracy of photometric redshifts is sufficient (Wolf et al. 2003).

To first order, photometric redshifts are reliable when the Balmer or Lyman continuum breaks can be observed between two broad band filters. Conventional optical filters from B to the I bands can therefore measure redshifts between $0.2 < z < 1$. In addition, near infrared data are required to provide robust photometric redshifts in the "redshift desert" at $z > 1.5$ since the Balmer break is redshifted to $\lambda > 10000$Å (Cimatti et al. 2002, Gabasch et al. 2004, Mobasher et al. 2004). Beyond $z > 3$, reliable photometric redshifts can be estimated using deep U or B band data, based on the Lyman break visible at $\lambda > 3600$Å (e.g. Madau 1995).

The reliability of photometric redshifts is also related to the photometric redshift method. In the standard χ^2 minimisation method, the most likely redshift and galaxy type are determined by a template-fitting procedure, which operates by fitting the observed photometric data with a reference set of spectral templates (e.g. Puschell 1982). Since no spectroscopic information is required, this standard χ^2 method can provide redshifts beyond the spectroscopic limit (Bolzonella et al. 2002). An alternative approach is to use a "training method" which can extract information from the spectroscopic sample to estimate the photometric redshifts. For example, neural network methods (e.g. Vanzella et al. 2004) or an empirical reconstruction of the redshift-colour relation (e.g. Connolly et al. 1995, Wang et al. 1998, Csabai et al. 2000). However, if the training set poorly samples the redshift range these methods can become unreliable. As a hybrid approach combining the advantages of both methods, the standard χ^2 method can be optimised using a spectroscopic sample. For instance, the initial template set can be optimised (Budavári et al. 2000, Benítez 2004) or the spectroscopic redshift distribution could be introduced as a "prior" in a Bayesian fitting procedure (Benítez 2000). Essentially, these techniques use the spectroscopic information to improve photometric redshift quality.

Until now, however, the major limiting factor in the successful exploitation of photometric redshifts has been our uncertain knowledge of just how reliable they actually are. Are there systematic trends between spectroscopic and photometric redshifts? What fraction of objects have 'catastrophic' errors (difference between photometric and spectroscopic redshifts largely greater than the expected uncertainty)? How the photometric redshift reliability is correlated with the galaxy spectral type and the apparent magnitude? Addressing these issues in a thorough manner requires both a large, highly uniform photometric sample free from systematic errors and a large, deep, spectroscopic sample of object selected in the simplest possible manner. Previous studies at $z > 0.3$ have been concerned either very deep small surveys or larger surveys but with correspondingly shallower areas. In all cases, the number of available spectroscopic redshifts has been small (typically less than $\sim 10^3$ objects). The combination of the high-throughput VIMOS wide-field spectrograph (Le Fèvre et al. 2003) and the MEGACAM survey camera at CFHT (Boulade et al. 2003) makes it possible to amass a large, deep, highly uniform photometric and spectroscopic samples.

In this paper we present photometric redshifts measured using the Canada-France Hawaii Telescope Legacy Survey "Deep Fields" catalogues (CFHTLS, *http://www.cfht.hawaii.edu/Science/CFHTLS*) processed at the TERAPIX data reduction centre[1] complemented with shallower VIMOS VLT Deep Survey multi-colour data (McCracken et al. 2003, Le Fèvre et al. 2004a). We use the current release 'T0003' of the CFHTLS. We focus on the deep field CFHTLS-D1 (or VVDS-0226-04) for which 11567 faint selected spectra $I_{AB} \leq 24.0$ are available from the VVDS spectroscopic survey (Le Fèvre et al. 2005a) and are used here as a training sample. We then compute photometric redshifts for all the CFHTLS "Deep Fields" D1, D2, D3, and D4 to obtain a large and deep dataset of 522286 objects at $i'_{AB} \leq 25$. Photometric and spectroscopic data are de-

Send offprint requests to: O. Ilbert, e-mail: olivier.ilbert1@bo.astro.it

⋆ Based on data obtained with the European Southern Observatory on Paranal, Chile, and on observations obtained with MegaPrime/Megacam, a joint project of CFHT and CEA/DAPNIA, at the Canada-France-Hawaii Telescope (CFHT) which is operated by the National Research Council (NRC) of Canada, the Institut National des Science de l'Univers of the Centre National de la Recherche Scientifique (CNRS) of France, and the University of Hawaii. This work is based in part on data products produced at TERAPIX and the Canadian Astronomy Data Centre as part of the Canada-France-Hawaii Telescope Legacy Survey, a collaborative project of NRC and CNRS.

[1] terapix.iap.fr

scribed in Section 2. Results derived with the standard χ^2 method are presented in Section 3. We describe in Section 4 how the standard χ^2 method can be calibrated using spectroscopic data. The quality of these calibrated photometric redshifts is described in Section 5, as a function of redshift, apparent magnitude and spectral type. In Section 6, we investigate how the combination of different bands affects the accuracy of our photometric redshifts. We finally present in Section 7 the photometric redshifts with $i'_{AB} \leq 25$ in the 4 CFHTLS deep fields. More detailed scientific studies such as the evolution of the angular correlation function or of the galaxy luminosity function will be deferred to forthcoming articles.

Throughout the paper, we use a flat lambda cosmology ($\Omega_m = 0.3$, $\Omega_\Lambda = 0.7$) and we define $h = H_0/100$ km s^{-1} Mpc^{-1}. Magnitudes are given in the AB system. Photometric and spectroscopic redshifts are denoted by zp and zs; Δz represents $zp - zs$.

2. Data description

2.1. CFHTLS multi-colour data

The MEGACAM deep multi-colour data described in this paper have been acquired as part of the CFHT Legacy Survey (CFHTLS) which is currently underway at the 3.6m Canada-France-Hawaii telescope. The MEGACAM camera consists of 36 CCDs of 2048×4612 pixel and covers a field-of-view of 1 deg^2 with a resolution of 0.186 arcsecond per pixel. The data covers the observed wavelength range 3500Å $< \lambda <$ 9400Å in the u^*, g', r', i', z' filters (Figure 1). We analyse the four deep CFHTLS fields CFHTLS-D1 (centred on $02^h25^m59^s - 04°29'40''$), CFHTLS-D2 ($10^h00^m28^s + 02°12'30''$), CFHTLS-D3 ($14^h19^m27^s + 52°40'56''$) and CFHTLS-D4 ($22^h15^m31^s - 17°43'56''$), focusing primarily on the CFHTLS-D1 field for which we have a large spectroscopic sample available from the VIMOS-VLT deep survey (VVDS). We use the release 'T0003' of the CFHTLS. The data processing of the CFHTLS "deep fields" is described in McCracken et al. (2006, in preparation). Considerable attention has been devoted in the TERAPIX pipeline to produce a photometric calibration which is as uniform as possible over all fields. Comparing the stellar locus in colour-colour planes in the final four stacks indicates the variation in absolute photometric zero points field-to-field is less than 0.03 magnitudes (McCracken et al. 2006, in preparation).

After removing the masked area, the effective field-of-view is about 0.79, 0.80, 0.83 and 0.77 deg^2 for CFHTLS-D1, D2, D3 and D4 respectively. In CFHTLS-D1, the catalogue reaches limiting magnitudes of $u^*_{AB} \sim 26.5$, $g'_{AB} \sim 26.4$, $r'_{AB} \sim 25.0$, $i'_{AB} \sim 25.9$ and $z'_{AB} \sim 25.0$ (corresponding to the magnitude limit at which we recover 50% of simulated stellar sources added to the images using our default detection parameters). The data in other CFHTLS "Deep Fields" are also extremely deep with a limiting magnitude $i'_{AB} \sim 25.7, 26.2, 26.0$ in the D2, D3, D4 respectively. A summary table listing the exposure times in each band is given on the TERAPIX web page (*http://terapix.iap.fr/*). Apparent magnitudes are measured using Kron-like elliptical aperture magnitudes (Kron 1980). The magnitudes are corrected from the galactic extinction estimated object by object from dust map images (Schlegel et al. 1998). We multiply all the SExtractor (Bertin & Arnouts 1996) flux error estimates by a factor of 1.5 to compensate for the slight noise correlation introduced by image re-sampling during the stacking of CFHTLS exposures.

2.2. VVDS multi-colour data

In addition to CFHTLS data on the CFHTLS-D1 field, we use the shallower images from the VVDS survey acquired with the wide-field 12K mosaic camera on the CFHT (Le Fèvre et al. 2004a). McCracken et al. (2003) describe in detail the photometry and the astrometry of the VVDS-0226-04 field. The VVDS-0226-04 field covers the entire CFHTLS-D1 deep field and reaches the limiting magnitudes $B_{AB} \sim 26.5$, $V_{AB} \sim 26.2$, $R_{AB} \sim 25.9$ and $I_{AB} \sim 25.0$ (corresponding to 50% completeness). Near infrared data in J and Ks bands are also available over 160 arcmin^2 with the magnitude limits of $J_{AB} \sim 24.1$ and $K_{AB} \sim 23.8$ respectively (Iovino et al. 2005).

2.3. VVDS spectroscopic data

We use the VVDS spectroscopic data acquired with the VIsible Multi-Object Spectrograph (VIMOS) installed at the ESO-VLT. In this paper, we consider the deep spectroscopic sample observed in the VVDS-0226-04 field (CFHTLS-D1) and selected according to the criterion $17.5 \leq I_{AB} \leq 24.0$ (Le Fèvre et al. 2005a). This sample comprises 11567 spectra. Four classes have been established to represent the quality of each spectroscopic redshift measurement, corresponding to confidence levels of 55%, 81%, 97% and 99% respectively (Le Fèvre et al. 2005a). Since our goal is to assess the quality of the photometric redshifts including the fraction of catastrophic failures, we restrict ourselves to the classes with a confidence level greater or equal to 97% (class 3 and 4). In the sub-area in common with the CFHTLS-D1 field, the final spectroscopic sample used in this paper consists in 2867 galaxies and 364 stars with highly reliable redshift measurements. The median redshift is about 0.76. The 1σ accuracy of the spectroscopic redshift measurements is estimated at 0.0009 from repeated VVDS observations.

2.4. Summary

To summarise, the multi-colour data on the CFHTLS-D1 field consists in two joint $u*$, g', r', i', z' and B, V, R,

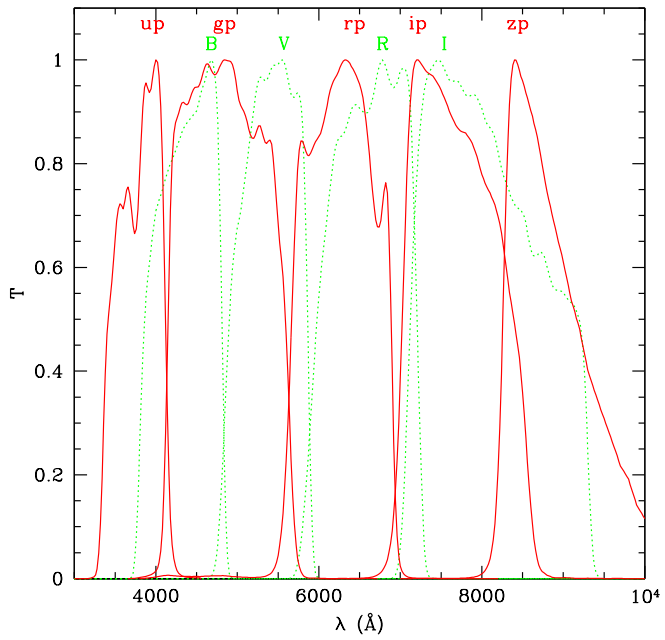

Fig. 1. CFHT transmissions curves normalised to unity. The solid lines correspond to the $u*$, g', r', i', z' MEGACAM filter curves; the dotted lines correspond to the B, V, R, I CFH12K curves.

I datasets over 0.79 deg^2, adding also J and K apparent magnitudes over 160 arcmin^2. For each object, the photometric redshift is computed using all the available bands. These photometric redshifts are calibrated using 2867 spectroscopic redshifts which have a confidence level greater or equal to 97%. As an illustration of our combined photometric and spectroscopic data set, Figure 2 shows the observed colours (using only CFHTLS filters) as a function of the spectroscopic redshifts. Multi-colour data in $u^*g'r'i'z'$ filters is also available on the other four fields.

3. Photometric redshifts with the standard χ^2 method

We present in this Section the results obtained with a standard χ^2 method, without training the photometric redshift estimate on the spectroscopic sample.

3.1. The photometric redshift code *Le_Phare*

We use the code *Le Phare*[2] (S. Arnouts & O. Ilbert) to compute photometric redshifts. The standard χ^2 method is described in Arnouts et al. (1999, 2002). These photometric redshifts have been found to agree well with computations from "Hyperz" (Bolzonella et al. 2000).

The observed colours are matched with the colours predicted from a set of spectral energy distribution (SED). Each SED is redshifted in steps of $\Delta z = 0.04$ and convolved with the filter transmission curves (including instrument efficiency). The opacity of the inter-galactic medium (Madau 1995) is taken into account. The merit function χ^2 is defined as

$$\chi^2(z,T,A) = \sum_{f=1}^{N_f} \left(\frac{F^f_{\rm obs} - A \times F^f_{\rm pred}(z,T)}{\sigma^f_{\rm obs}} \right)^2 , \qquad (1)$$

where $F^f_{\rm pred}(T,z)$ is the flux predicted for a template T at redshift z. $F^f_{\rm obs}$ is the observed flux and $\sigma^f_{\rm obs}$ the associated error. The index f refers to the considered filter and N_f is the number of filter. The photometric redshift is estimated from the minimisation of χ^2 varying the three free parameters z, T and the normalisation factor A.

3.2. Template set

Our primary template set are the four Coleman Wu and Weedman (CWW) observed spectra: Ell, Sbc, Scd, Irr (Coleman, Wu & Weedman 1980) commonly used to estimate the photometric redshifts (Sawicki et al. 1997, Fernández-Soto et al. 1999, Arnouts et al. 1999, Brodwin et al. 2006). We add an observed starburst SED from Kinney et al. (1996) to make our template sets more representative. These templates are linearly extrapolated into ultraviolet ($\lambda < 2000$Å) and near-infrared wavelengths using the GISSEL synthetic models (Bruzual et Charlot 2003). For spectral types later than Sbc, we introduce a reddening $E(B-V) = 0, 0.05, 0.1, 0.15, 0.2$ which follows the interstellar extinction law measured in the Small Magellanic Cloud (Prevot et al. 1984). Even if these five templates are not completely representative of the variety of observed spectra, it does reduce the possible degeneracies between predicted colours and redshift (Benítez 2000).

3.3. Results based on the standard χ^2 method

We first apply the standard χ^2 method on the CFHTLS-D1 data without incorporating any spectroscopic information. Figure 3 shows a comparison between the VVDS spectroscopic redshifts and the photometric redshifts at $i' \leq 22.5$. A clear systematic offset is visible at $zs < 0.5$. We would not expect such a trend to appear for such a relatively bright sample in a redshift range where the Balmer break is between our u^* and the r' filters. Small uncertainties in the photometric zero-point calibration or an imperfect knowledge of the complete instrument transmission curve are probably responsible for this trend.

At fainter magnitudes (top left panel of Figure 6, method *a)*), we see there are a large number of galaxies with $\Delta z > 1$, mainly in the redshift range $1.5 < zp < 3$. Most of these catastrophic errors are caused by misidentification of Lyman and Balmer break features. An illustration of this degeneracy is presented in Figure 4, which demonstrates the importance of near-infrared data

[2] www.lam.oamp.fr/arnouts/LE_PHARE.html

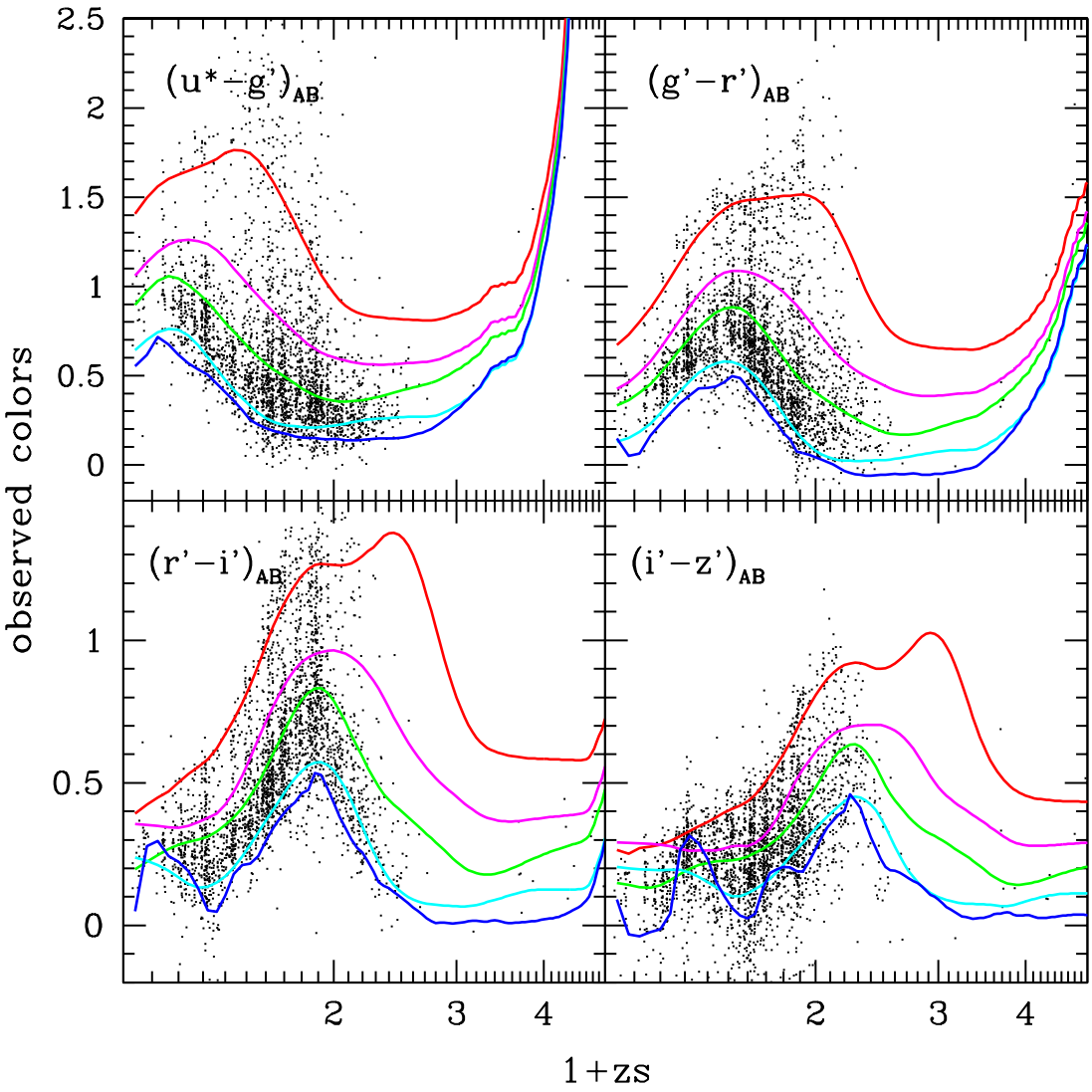

Fig. 2. Observed colours as a function of the spectroscopic redshifts (black points). The predicted colours derived from our optimised set of templates (see section 4.2) are shown with solid lines: Ell (red), Sbc (magenta), Scd (green), Irr (cyan) (Coleman, Wu & Weedman 1980) and starburst (dark blue) (Kinney et al. 1996) from the top to the bottom, respectively.

to break this degeneracy. An alternative solution is to include a relevant information in the redshift probability distribution function (PDFz) using the Bayesian approach (e.g. Benítez 2000, Mobasher et al. 2004) in order to favour one of the two solutions, as is discussed in Section 4.3.

This basic comparison shows that blindly trusting the accuracy of photometric redshifts is perilous. In the following, we will improve the photometric redshift quality using a spectroscopic training set.

4. An improved method to compute robust photometric redshifts

As we demonstrated in Section 3.3, spectroscopic redshifts are required to calibrate the standard χ^2 method. In this Section, we describe the steps we have followed to calibrate the χ^2 photometric redshift estimate.

4.1. Systematic offsets

We first select a control sample of 468 very bright galaxies ($i'_{AB} \leq 21.5$) which have spectroscopic redshifts. Using a χ^2 minimisation (equation 1) at fixed redshift, we determine for each galaxy the corresponding best-fitting CWW template. We note in each case F^f_{obs} the observed flux in the filter f and F^f_{pred} the predicted flux derived from the best-fit template. For each filter f, we minimise the sum

$$\psi^2 = \sum_{i' \leq 21.5}^{Ngal} \left((F^f_{\rm pred} - F^f_{\rm obs} + s^f)/\sigma^f_{\rm obs} \right)^2$$

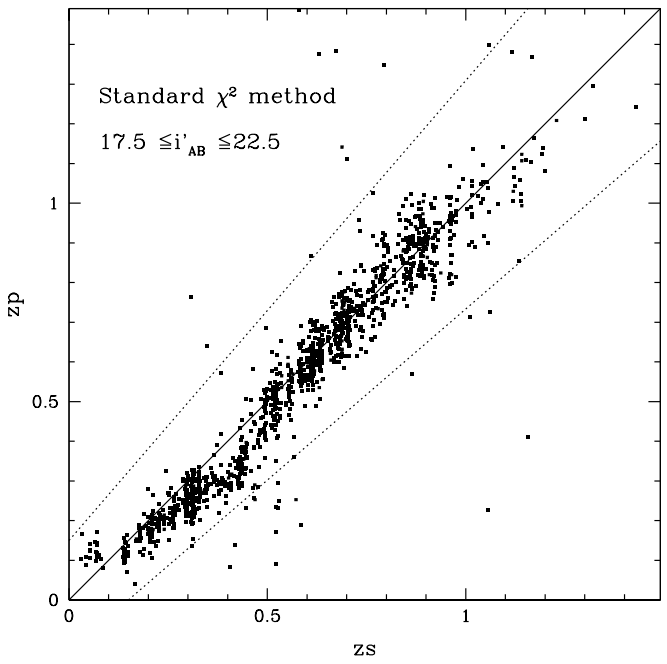

Fig. 3. Comparison between spectroscopic and photometric redshifts determined with the standard χ^2 method (without adding the spectroscopic information) for a bright selected sample $17.5 \leq i'_{AB} \leq 22.5$.

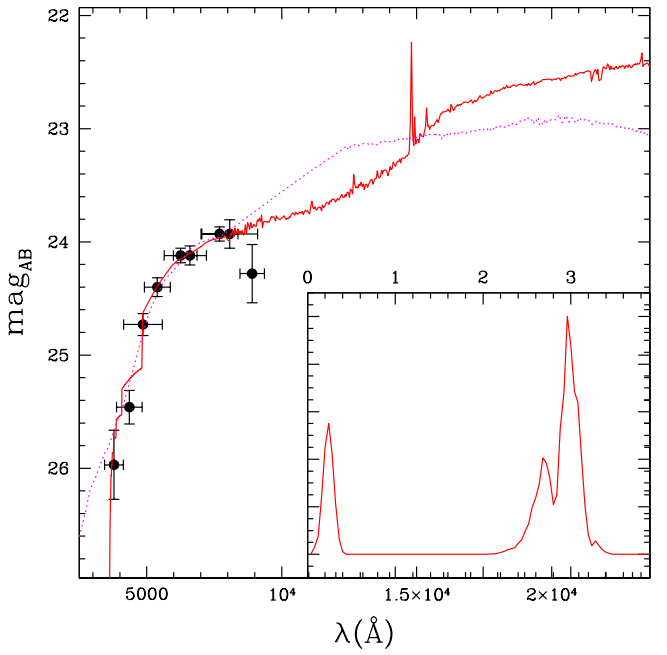

Fig. 4. Example of best-fitted templates on multi-colour data for a galaxy at $zs = 0.311$. The solid black points correspond to the apparent magnitudes in the $u^*, B, g', V, r', R, i', I, z'$ filters from the left to right respectively. The solid line corresponds to a template redshifted at $zp = 2.97$ and the dotted line at $zp = 0.24$. The enclosed panel is the associated Probability Distribution Function (PDFz).

filter	CWW $i'_{AB} < 20.5$	CWW $i'_{AB} < 21.5$	CWW $i'_{AB} < 22.5$	PEGASE $i'_{AB} < 21.5$
u^*	+0.044	+0.045	+0.041	+0.066
g'	-0.080	-0.080	-0.079	-0.087
r'	+0.011	-0.006	-0.012	-0.002
i'	-0.005	-0.002	-0.004	-0.001
z'	-0.037	-0.025	-0.014	-0.045
B	+0.057	+0.067	+0.074	+0.063
V	-0.066	-0.062	-0.059	-0.066
R	+0.098	+0.086	+0.083	+0.096
I	-0.022	-0.001	-0.002	-0.012

Table 1. Systematic differences s^f between observed and predicted apparent magnitudes. These values are given for the set of CWW templates and for different cuts in apparent magnitudes. We add also the values obtained with the synthetic library PEGASE. Throughout the paper, we use the values quoted for CWW $i'_{AB} < 21.5$.

leaving s^f as a free parameter. For normal uncertainties in the flux measurement, the average deviation s^f should be 0. Instead, we observe some systematic differences which are listed in Table 1. Such differences have already been noted by Brodwin et al. (2006) in the Canada-France Deep Fields Survey. In our data, these differences never exceed 0.1 magnitude and have an average amplitude of 0.042 magnitude. They depend weakly on the magnitude cut adopted to select the bright sub-sample (Table 1) and are also weakly depending on the set of templates (see Table 1 with the values obtained using the synthetic library PEGASE Fioc & Rocca-Volmerange 1997). Uncertainties in the calibration of the photometric zero-points may create discontinuities not reproduced by the templates. The size of these systematic differences are compatible with the expected uncertainties in the absolute zero-point calibration (0.05 magnitudes).

We then proceed to correct the predicted apparent magnitudes from these systematic differences. s^f is the estimated correction that we apply to the apparent magnitudes in a given filter f. If we repeat a second time the procedure of template-fitting after having adjusted the zero-points, the best-fit templates may change. We check that the process is converging: after three iterations the estimated corrections s^f vary less than 2%. The values listed in the Table 1 are measured after 3 iterations. Differently from Brodwin et al. (2006), the corrections used to correct the apparent magnitudes are obtained only on a bright sub-sample ($i' \leq 21.5$) after 3 iterations. Since the uncertainties in the zero-point calibration are not better than 0.01, we add 0.01 in quadrature to the apparent magnitude errors.

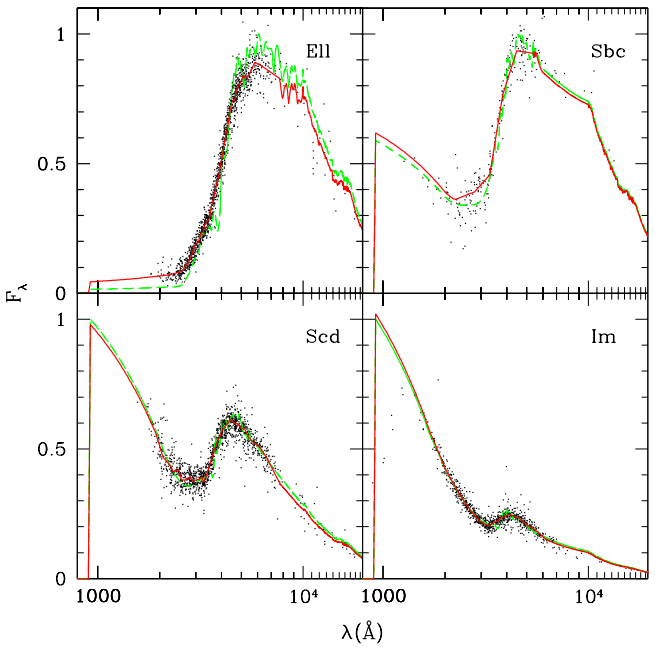

Fig. 5. Each panel corresponds to one of the four CWW templates (Ell, Sbc, Scd, Irr). The points correspond to the flux of each galaxy redshifted to the rest-frame using the spectroscopic redshifts. The green dashed lines are the initial SEDs and the red solid lines are the optimised SEDs which are the output of the procedure described in section 4.2.

4.2. Template optimisation

The apparent magnitude measured in the filter λ_{eff} provides the rest-frame flux at $\lambda_{eff}/(1+z_i)$ for a galaxy with a spectroscopic redshift z_i. Since all the galaxies are at different redshifts, we can estimate the rest-frame flux over a continuous range of rest-frame wavelengths from the spectroscopic sample. In this way can we optimise our set of CWW templates.

We split the galaxy spectroscopic sample according to the best-fit template (4 CWW + a starburst template with a possible additional extinction). Keeping only the objects fitted without additional extinction, we use a sub-sample of 309 galaxies to perform the template optimisation. The black points in Figure 5 show the rest-frame flux reconstructed from observed apparent magnitudes. We observe a slight deviation between these points and the initial templates (dashed lines), particularly for early spectral type galaxies. We sort the rest-frame flux according to their wavelengths and bin them by group of 50 points. To produce the optimised templates, we connect the median flux in each bin (solid lines). When no data are available, we keep the extrapolation provided by the initial set of templates. We don't optimise the starburst template to keep the emission lines in this template.

The colours predicted for these five main optimised templates are displayed as a function of redshift in Figure 2. The observed trend in the colour-redshift relation are well reproduced by our set of templates. For $r'-i'$ and $i'-z'$ colours, we observe oscillations of the predicted colour-redshift relation for the starburst template. These oscillations are explained by the contribution of emission lines like H_α and OIII to the observed flux. Since we use only one starburst template to constrain the possible degeneracies in colour-redshift space, we are not covering the broad range of possible intensities and line ratios. In particular, we do not reproduce some blue observed colours $(r'-i')_{AB} < 0.1$ and $(i'-z')_{AB} < 0$ (Figure 2). This lack of representativeness which we have adopted to avoid degeneracies leads to an accumulation of photometric redshifts in certain peaks of the colour-redshift relation, for galaxies with strong emission lines. This is responsible for the presence of narrow peaks in the redshift distribution for the starburst spectral types.

Finally, these five main optimised templates are linearly interpolated to produce a total of 62 templates to improve the sampling of the redshift-colour space and therefore the accuracy of the redshift measurement.

4.3. Bayesian approach

The Bayesian approach (Benítez 2000) allows us to introduce a relevant *a priori* information in the PDFz. Following the formalism developed by Benítez (2000), we introduce the prior

$$p(z,T|i'_{AB}) = p(T|i'_{AB})p(z|T,i'_{AB}) \quad (2)$$

with $p(z|T,i'_{AB})$ the redshift distribution and $p(T|i'_{AB})$ the probability to observe a galaxy with the spectral type T. $p(z|T,i'_{AB})$ is parametrised as:

$$p(z|T,i'_{AB}) \propto z^{\alpha_t} exp\left(-\left[\frac{z}{z_{0t}+k_{mt}(i'_{AB}-20)}\right]^{\alpha_t}\right), \quad (3)$$

and $p(T|i'_{AB})$ as:

$$p(T|i'_{AB}) \propto f_t e^{-k_t(i'_{AB}-20)}. \quad (4)$$

The subscript t denotes the type dependency. Using the formalism adopted in Benítez (2000), we recompute the values of the free parameters using the VVDS redshift distribution. We split the sample according to the four optimised CWW templates. We adjust the parameters α_t, z_{0t}, k_{mt} to maximise the likelihood of "observing" the VVDS spectroscopic sample. We use the MINUIT package of the CERN library (James & Roos 1995) to perform the maximisation (MIGRAD procedure) and to obtain the corresponding errors (MINOS procedure). The values of these parameters for each type are presented in Table 2. The parameters f_t and k_t are also given in Table 2 for types one, two, and three and the fraction of type four is automatically set to complete the sample.

spectral type	α_t	z_{0t}	k_{mt}	f_t	k_t
Ell	$3.331^{+0.109}_{-0.108}$	$0.452^{+0.015}_{-0.015}$	$0.137^{+0.007}_{-0.007}$	$0.432^{+0.047}_{-0.047}$	$0.471^{+0.043}_{-0.043}$
Sbc	$1.428^{+0.081}_{-0.080}$	$0.166^{+0.024}_{-0.023}$	$0.129^{+0.013}_{-0.013}$	$0.080^{+0.021}_{-0.021}$	$0.306^{+0.098}_{-0.098}$
Scd	$1.583^{+0.038}_{-0.038}$	$0.211^{+0.015}_{-0.014}$	$0.140^{+0.006}_{-0.006}$	$0.312^{+0.033}_{-0.033}$	$0.127^{+0.036}_{-0.036}$
Irr	$1.345^{+0.021}_{-0.021}$	$0.204^{+0.014}_{-0.014}$	$0.138^{+0.005}_{-0.005}$	...	...

Table 2. Parameters used for the prior $P(z, T|i'_{AB})$ using the formalism from Benítez (2000). These parameters are derived from the VVDS spectroscopic sample.

4.4. Summary

The photometric redshifts are estimated using the code *Le Phare*[3] (S. Arnouts & O. Ilbert). We calibrate the standard χ^2 method using the VVDS spectroscopic redshifts:

- We first adjust iteratively the zero-points of the multi-colour catalogue using a bright spectroscopic sample.
- Then we optimise our primary set of templates using the observed flux rest-frame shifted at $\lambda/(1+z_i)$.
- Finally we apply a prior based on the VVDS redshift distribution following the Bayesian formalism presented in Benítez (2000).

5. Results: photometric redshift accuracy

We now assess the quality of the photometric redshifts obtained with the calibration method described in Section 4, by comparing the spectroscopic and photometric redshift samples on the CFHTLS-D1.

5.1. Method improvement

Figure 6 shows the photometric redshifts versus the spectroscopic redshifts for different steps in the calibration method. The systematic trends observed with the standard χ^2 method (top left panel, method *a)*) are removed by the template optimisation and the systematic offset corrections (top right panel, method *b)*). After this step, the accuracy reaches $\sigma_{\Delta z/(1+zs)} = 0.037$. Adding a prior on the redshift distribution decreases the fraction of catastrophic errors without creating any systematic trends (bottom left panel, method *c)*). The final fraction of catastrophic errors has decreased by a factor 2.3. In the following, we restrict our analysis to the best method *c)*. This comparison shows the essential role of the spectroscopic information to build a robust photometric redshift sample.

With our final calibration method, we reach an accuracy $\sigma_{\Delta z/(1+zs)} = 0.037$. At $i'_{AB} \leq 24$, we recover 96% of the galaxies in the redshift range $|\Delta z| < 0.15(1+zs)$. $\sigma_{\Delta z/(1+zs)} = 0.037$ is similar to the accuracy obtained by the COMBO-17 survey with a larger set of medium band filters (Wolf et al. 2004). However, considerations on the quality of photometric redshifts derived from statistical measurements using the whole sample are not really meaningful since such statistics depends on the apparent magnitude, the spectral type and the redshift range. We investigate these dependencies in the next Section.

[3] www.lam.oamp.fr/arnouts/LE_PHARE.html

5.2. Dependency on apparent magnitude, spectral type and redshift

Figure 7 shows the comparison between photometric and spectroscopic redshifts as a function of apparent magnitude. The fraction of catastrophic errors η increases by a factor of 12 going from $17.5 \leq i'_{AB} \leq 21.5$ up to $23.5 \leq i'_{AB} \leq 24$. The redshift rms increases continuously from $\sigma_{\Delta z/(1+zs)} \sim 0.028$ up to $\sigma_{\Delta z/(1+zs)} \sim 0.048$. The apparent magnitude is therefore a key parameter, which is to be expected as the template fitting is less constrained for the fainter objects.

Figure 8 shows the comparison between photometric and spectroscopic redshifts as a function of the spectral type. We define the spectral type according to the best-fit template. The fraction of catastrophic errors η increases by a factor of seven from the elliptical to the starburst spectral types. The starburst galaxies represent 18% of the spectroscopic sample but 54% of the catastrophic errors. The accuracy in the redshift measurement is similar for the Ell, Sbc, Scd and Irr spectral types with $\sigma_{\Delta z/(1+zs)} = 0.032 - 0.036$ but rises to $\sigma_{\Delta z/(1+zs)} = 0.047$ for the starburst galaxies. Such a dependency on the spectral type is expected since the robustness of the photometric redshifts relies strongly on the strength of Balmer break, which is weaker for later types. In addition, the photometric redshift estimate of late spectral type galaxies is affected by the intrinsic dispersion in the properties of the emission lines and by the large range in intrinsic extinction.

The photometric redshift reliability also depends on the considered redshift range. We quantify the dependency on the redshift in Figure 9 and Figure 10 showing the rms scatter $\sigma_{\Delta z/(1+zs)}$ and the fraction of catastrophic errors η as a function of redshift up to $z = 1.5$. We split the sample into a bright $17.5 \leq i'_{AB} \leq 22.5$ and a faint $22.5 \leq i'_{AB} \leq 24$. We choose the limit $i'_{AB} = 22.5$ since it corresponds to the depth of the shallow VVDS and zCOSMOS spectroscopic surveys. The fraction of catas-

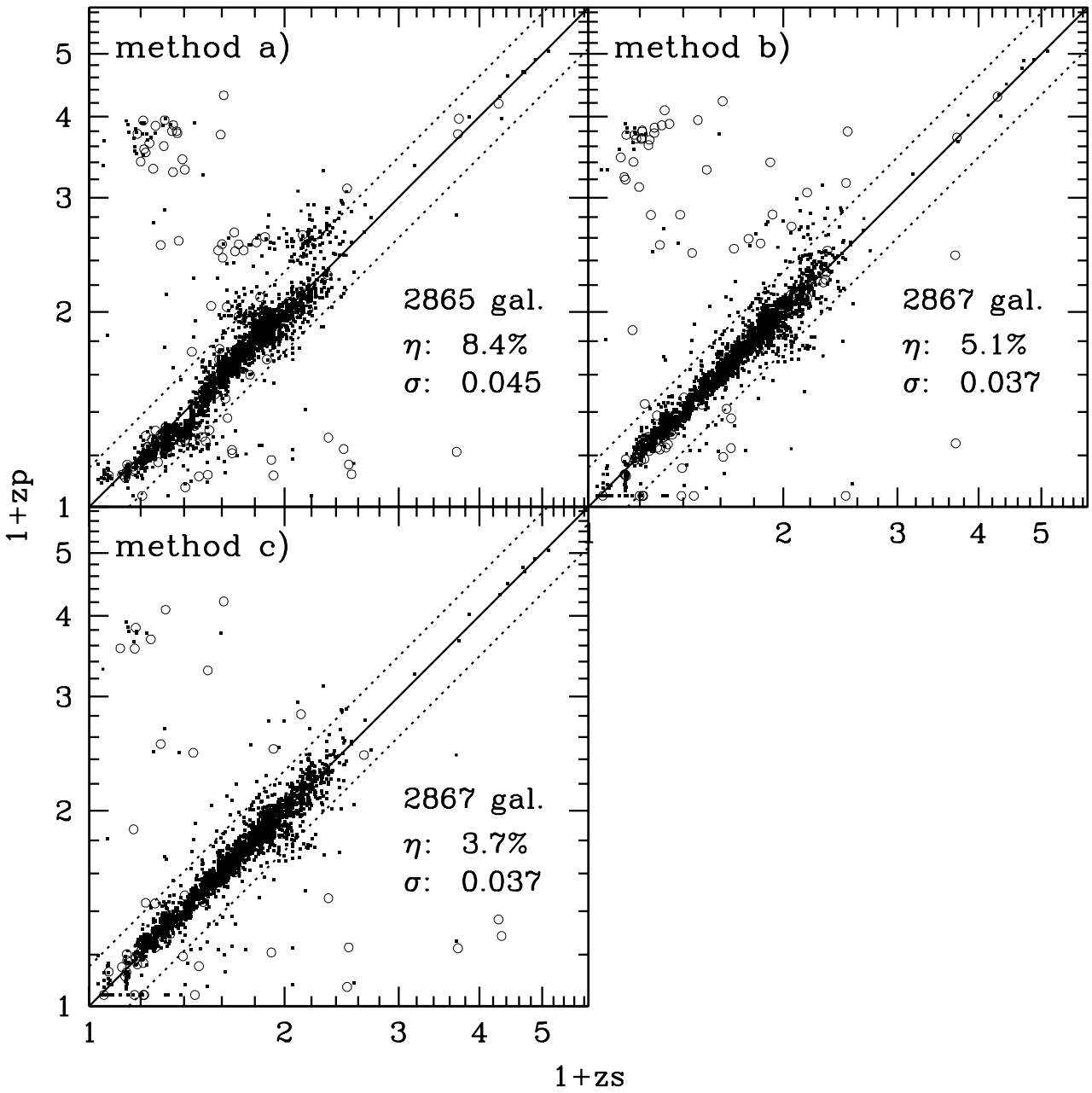

Fig. 6. Photometric redshifts versus spectroscopic redshifts for the sample $17.5 < i'_{AB} < 24$. Each panel corresponds to an additional step in the calibration method with: *method a*) the standard χ^2 method ; *method b*) adding the templates optimisation and the corrections of the systematic offsets ; *method c*) our best method using the Bayesian approach, the templates optimisation and the corrections of systematic offsets. The solid line corresponds to $zp = zs$. The dotted lines are for $zp = zs \pm 0.15(1 + zs)$. We quote as catastrophic errors the fraction η of galaxies with $|zs - zp|/(1 + zs) > 0.15$ and the accuracy $\sigma_{\Delta z/(1+zs)}$. The open symbols correspond to galaxies with a second peak detected in the PDFz (probability threshold at 5%).

trophic errors increases dramatically only at $z < 0.2$. At $0.2 \leq z \leq 1.5$, the accuracy is always better than $0.045(1+zs)/0.55(1+zs)$ for the bright and faint samples respectively. The fraction of catastrophic errors η remains always less than $\sim 4\%/14\%$ for the bright and faint sample respectively (Figure 10). We observe a degeneracy for $zs < 0.4$ and $1.5 < zp < 3$ faint galaxies (bottom left panel of Figure 6). The origin of this degeneracy is a mismatch between the Balmer break and the intergalactic Lyman-alpha forest depression at $\lambda < 1216$Å. 70% of the galaxies at $1.5 < zp < 3$ are in fact at $zs < 0.4$ which prevents the use of this spectral range. At $zs > 3$, the Lyman Break is observed between the u^* band and the g' bands, allowing a reliable photometric redshift estimate for Lyman Break

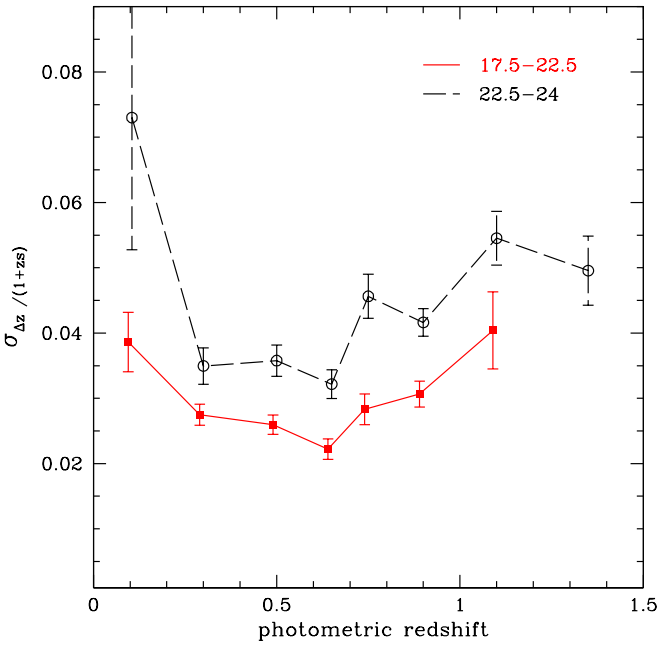

Fig. 9. Accuracy of the photometric redshifts as a function of redshift. Catastrophic errors are removed from the sample. Only bins with more than ten objects are shown.

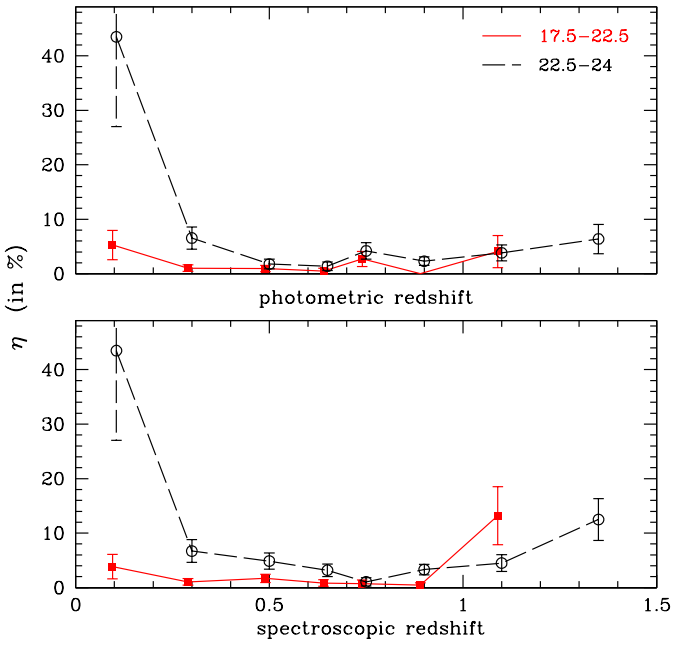

Fig. 10. Fraction of catastrophic errors η per redshift bins. The catastrophic errors are defined as galaxies with $|zs - zp|/(1 + zs) > 0.15$. The fraction is measured as a function of the photometric redshift (top panel) and of the spectroscopic redshift (bottom panel). The top panel shows the level of contamination, i.e. the fraction of wrong redshifts in a given photometric redshift slice. The bottom panel shows the level of incompleteness, i.e. the fraction of redshifts not recovered in a given photometric redshift slice. Only bins with more than ten objects are shown.

galaxies. We recover 6 of the 8 galaxies at $zs > 3$ (bottom left panel of Figure 6). Even if the quality of the photometric redshifts appears good, we point out that we are using only spectroscopic redshifts with the highest confidence level which is a specific population easier to isolate both in photometry and in spectroscopy since they have a significant Lyman break (Le Fèvre et al. 2005b). Moreover, we have tuned the calibration method to be efficient at $z < 1.5$ using a prior on the redshift distribution (see Section 4.3) and without allowing galaxies to be brighter than $M_{B_{AB}} = -24$ (Ilbert et al. 2005). We conclude that the most appropriate redshift range for forthcoming scientific analysis on the complete population of galaxies is $0.2 < zp < 1.5$.

5.3. Error analysis

We investigate here the reliability of the error associated to the photometric redshift estimate.

The redshift Probability Distribution Function (see Arnouts et al. 2002) is directly derived from the χ^2 distribution

$$PDFz = B \exp\left(-\frac{\chi^2(z)}{2}\right), \quad (5)$$

with B a normalisation factor. *Le_Phare* (S. Arnouts & O. Ilbert) produces the PDFz for each object. A second redshift solution is likely when a second peak is detected in the PDFz above a given threshold. An example of galaxy with the good redshift solution enclosed in the second peak of the PDFz is shown in Figure 4. The galaxies with a second peak in the PDFz are flagged with open circles in Figure 6, Figure 7, Figure 8 and make up for a large fraction of the catastrophic errors. We find that the fraction of catastrophic errors increases dramatically in those cases: when a second peak is detected with a probability greater than 5% the fraction of catastrophic errors increases to $\eta = 42\%$. Removing these galaxies from the sample could be useful to select the most robust sub-sample.

The error bars on the photometric redshifts are given by $\chi^2(z) = \chi^2_{min} + \Delta\chi^2$. $\Delta\chi^2 = 1$ and $\Delta\chi^2 = 9$ are used to compute the error bars at 1σ and 3σ respectively. Figure 11 shows the estimated error bars at 3σ in narrow bins of apparent magnitudes. The size of the error bar increases towards faint apparent magnitudes, in a consistent way with the Δz rms. We find that 67% and 90% of the spectroscopic redshifts are well located in the 1σ and 3σ error bars respectively. We note that these values remain lower than the theoretical values since photometric uncertainties (such as blending or the presence of bright neighbours) or the suitability of our template set are not taken into account in the computation of the PDFz. We conclude that our 1σ error bars are an accurate representation of the photometric redshift error, and there can be

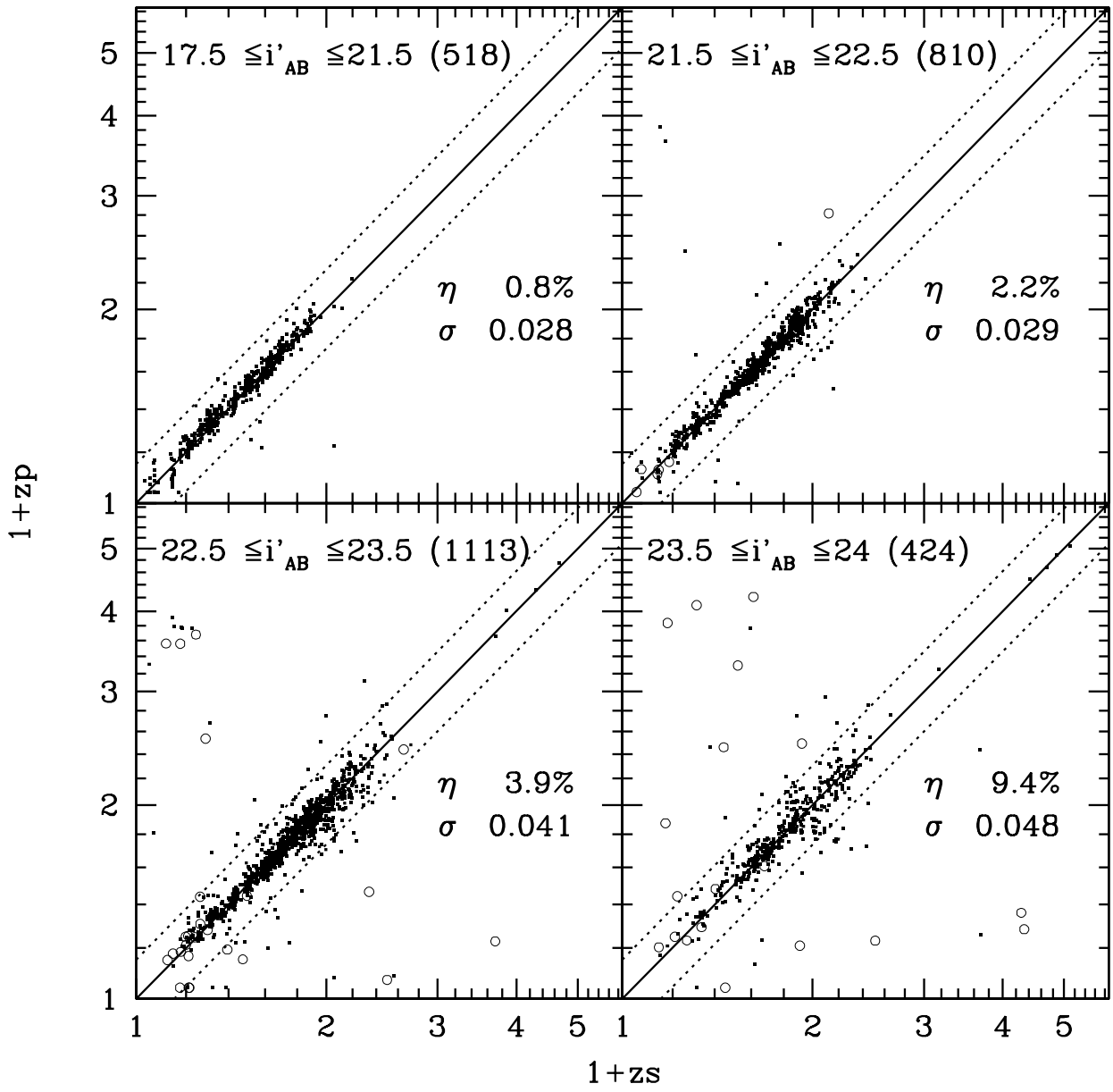

Fig. 7. Same as Figure 6 with the final calibration method *c)*. Each panel corresponds to a different selection in apparent magnitude.

a useful way to assess their reliability beyond the spectroscopic limit.

5.4. Comparison between photometric and spectroscopic redshift distributions

In order to calculate the galaxy redshift distribution, we first need to remove the stars from the sample. We use the half-light radius $r_{1/2}$, a morphological criterion measured provided by SExtractor (Bertin & Arnouts 1996). From the spectroscopic sample, we find that 95% of the stars have $r_{1/2} < 2.7$. Since 16% of the galaxies have also $r_{1/2} < 2.7$, we combine this morphological criterion with a colour criterion. For each object, we compute simultaneously the χ^2 for the galaxy library and the χ^2_s for the star library (Pickles 1998). If the conditions $\chi^2 - \chi^2_s > 0$ and $r_{1/2} < 2.7$ are satisfied simultaneously, the object is flagged as a star. Applying these criteria on the spectroscopic sample, we recover 79% of the stars and only 0.77% galaxies are misclassified as stars. The remaining 21% of stars are misclassified as galaxies and 69% of these are in the redshift range $zp < 0.2$.

Since we use the spectroscopic redshift distribution as a prior (see Section 4.3) a critical point is to check at which

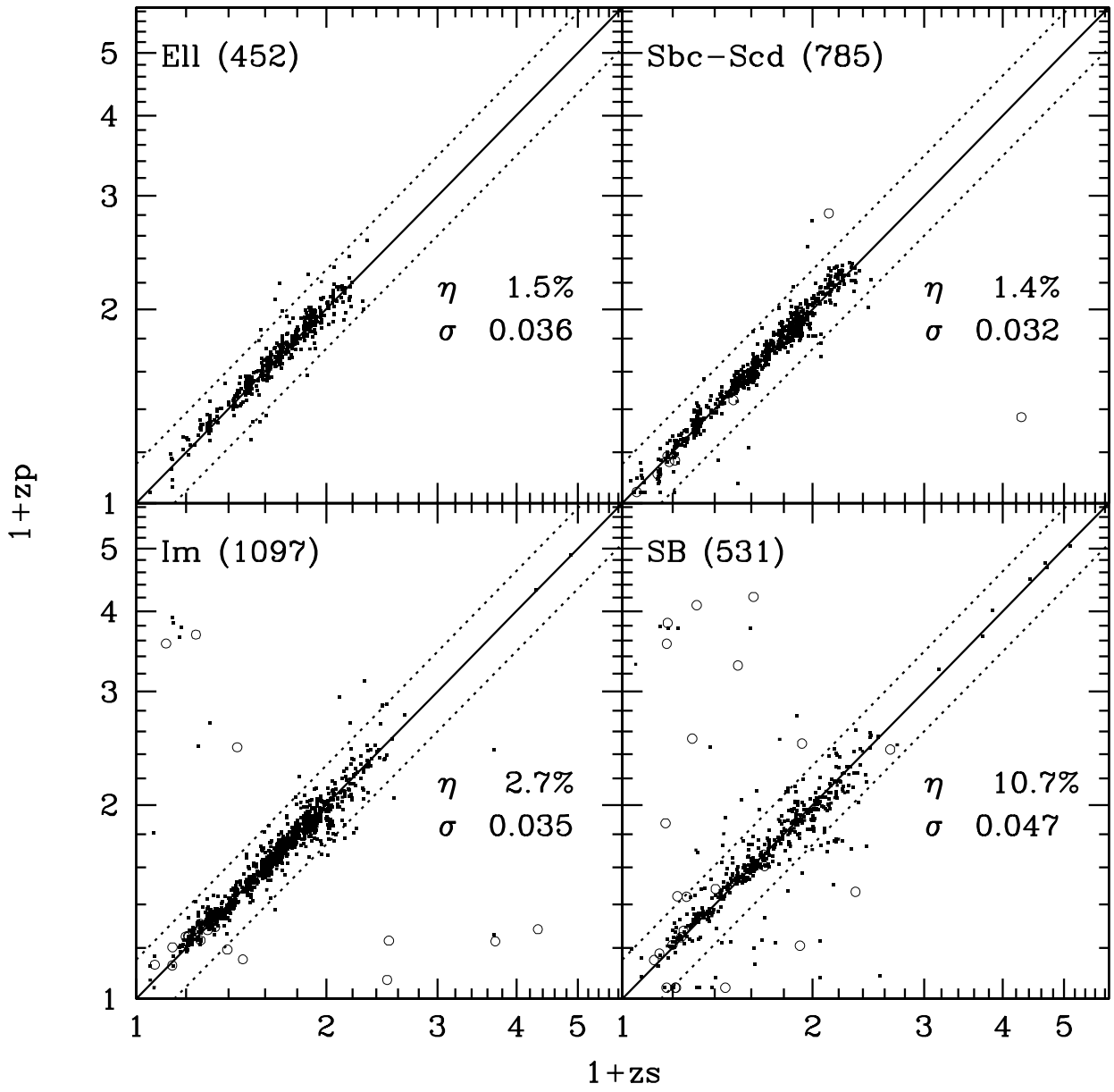

Fig. 8. Same as Figure 6 with our final calibration method *c)*. The sample is selected at $17.5 \leq i'_{AB} \leq 24$. Each panel corresponds to a different selection in spectral type defined according to the best-fitting template.

level the photometric redshift distribution depends on the prior. We compare the redshift distributions obtained using the prior (weighted solid lines) and without (dashed lines) in Figure 12. The prior has no impact on the global shape of the redshift distribution. We see significant differences in the redshift distributions at $z > 1.5$, where the prior efficiently removes the catastrophic failures at $1.5 < zp < 3$.

For the $i'_{AB} \leq 23$ and the $i'_{AB} \leq 24$ selected samples, we compare in Figure 12 the photometric and the VVDS spectroscopic redshift distributions. The distributions are in excellent agreement to $z \sim 1.5$. At $1.5 < z < 3$, the photometric redshifts are contaminated by low redshift galaxies (see Section 5.2) and the paucity of spectral features in UV makes spectroscopic redshift measurement difficult (Le Fèvre et al. 2005a). Both effects explain the difference between the photometric and spectroscopic redshift distribution at $z > 1.5$.

We are able to identify peaks in the photometric redshift distribution which are clearly associated with peaks in spectroscopic redshift distribution. We smooth the spectroscopic and photometric redshift distributions using a sliding window with a step $\Delta z = 0.2$. The ratio between the observed redshift distribution obtained with

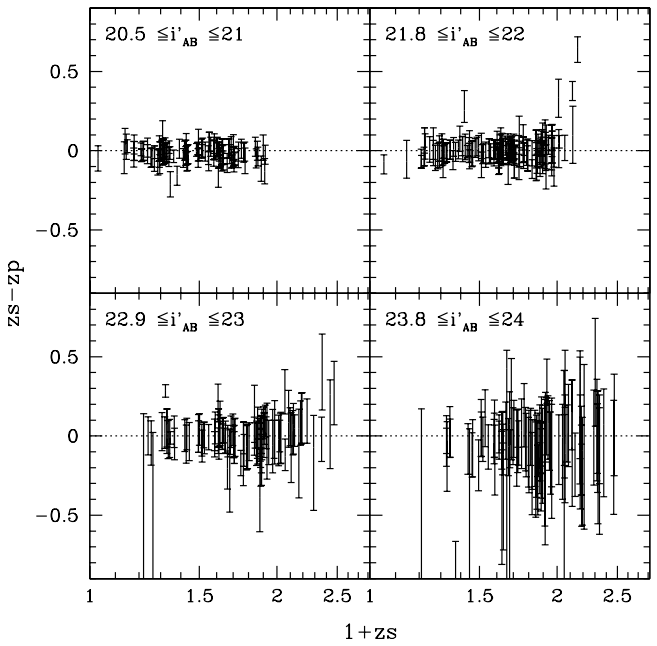

Fig. 11. Δz as a function of redshift in four apparent magnitude bins (shown for clarity). We report the 3σ error bars on the photometric redshift estimate.

a step $\Delta z = 0.01$ and the smoothed redshift distribution shows three peaks at $zp \sim 0.31, 0.61, 0.88$ in the photometric redshift distribution, in excellent agreement with peaks identified at $zs \sim 0.33, 0.60, 0.89$ in the spectroscopic redshift distribution. The significance of the peaks is lower by a factor two in the photometric redshift sample since the peaks are broadened by the uncertainties on the photometric redshift estimates.

6. Added value of each multi-colour data set

We now compare the reliability of photometric redshifts computed from either a $BVRI$ dataset using the VVDS-CFH12K photometry or $u^*g'r'i'z'$ using the CFHTLS-MEGACAM, and quantify the useful range of photometric redshifts for each of these datasets. In addition, we explore the added value of different bands to the accuracy and reliability of photometric redshifts.

6.1. Added value of u^* and z' bands

Removing successively the u^* and the z' bands, we investigate possible systematic trends if these bands are not available or if they are shallower.

Figure 13 (top left-hand panel) shows the photometric redshifts computed without u^* band data. Only $\sim 70\%$ of the photometric redshifts at $zs < 0.4$ are recovered which should be compared with $\sim 90\%$ using the u^* band. Since the filter system is no longer sensitive to the Lyman break, a large fraction of low redshift galaxies contaminates the $zp > 3$ redshift range. This test shows the importance of a deep u^* band to constrain the photometric redshifts at $z < 0.4$ and $z > 3$.

Figure 13 (top right panel) shows the photometric redshifts computed without z^* band data. Most of the photometric redshifts at $zs > 1$ are estimated at $zp \leq 1$. We observe an accumulation of photometric redshifts around $zp \sim 0.8 - 0.9$. This trend is expected since the filter system is no longer sensitive to the Balmer break at $z > 1$. In this case the use of the photometric redshifts is problematic even at $z < 1$ without z' band data.

6.2. Photometric redshifts from the VVDS imaging survey alone

The VVDS multi-colour survey was carried out in B, V, R and I bands over 10 deg^2 (Le Fèvre et al. 2004a) using the CFH12K wide-field mosaic camera at CFHT. The accuracy of the photometric redshifts using only BVRI is presented in Figure 13 (bottom right panel). Since the VVDS photometric survey is shallower, the quality of the photometric redshifts is obviously worse than the results presented previously. η rises to 19.1% which is a factor of five greater than our best value. As we demonstrate in Section 6.3, the absence of deep u^* and z' band data makes it difficult to compute photometric redshifts at $zs < 0.4$ and $zs > 1$. However, even using only four broad bands, we recover 80% of the spectroscopic redshifts at $I_{AB} \leq 24$ with $\sigma_{|\Delta z|/(1+zs)} = 0.057$.

6.3. Photometric redshifts from the CFHTLS imaging data alone

The deep CFHTLS survey consists in four fields imaged over 3.2 deg^2 in the $u^*g'r'i'z'$ filters. The quality of the photometric redshifts computed using only the $u^*g'r'i'z'$ bands is displayed in Figure 14 (top panel) for the CFHTLS-D1. We find $\eta = 4.2\%$ and $\sigma_{|\Delta z|/(1+zs)} = 0.040$. These CFHTLS photometric redshifts are close to be as accurate as the photometric redshifts computed using the full photometric dataset. Photometric redshifts for the other CFHTLS deep fields will be introduced in Section 7.

6.4. The near-infrared sample

Deep near-infrared observations in the J and K bands are available for a 160 arcmin^2 (Iovino et al. 2005) subarea of the D1 field. This complete sub-sample of 3688 galaxies at $K_{AB} \leq 23$ represents a unique dataset in term of depth and area (it is one magnitude deeper and covers a three times larger area than the K20 survey, Cimatti et al. 2002). Near-infrared bands are crucial to constrain the photometric redshifts in the 'redshift desert' since the J band is sensitive to the Balmer break up to $z \sim 2.5$ and enters in the K band at $z > 3.8$. The photometric redshifts for galaxies selected at $K_{AB} < 23$ are shown in Figure 13 (bottom left panel). We obtain the

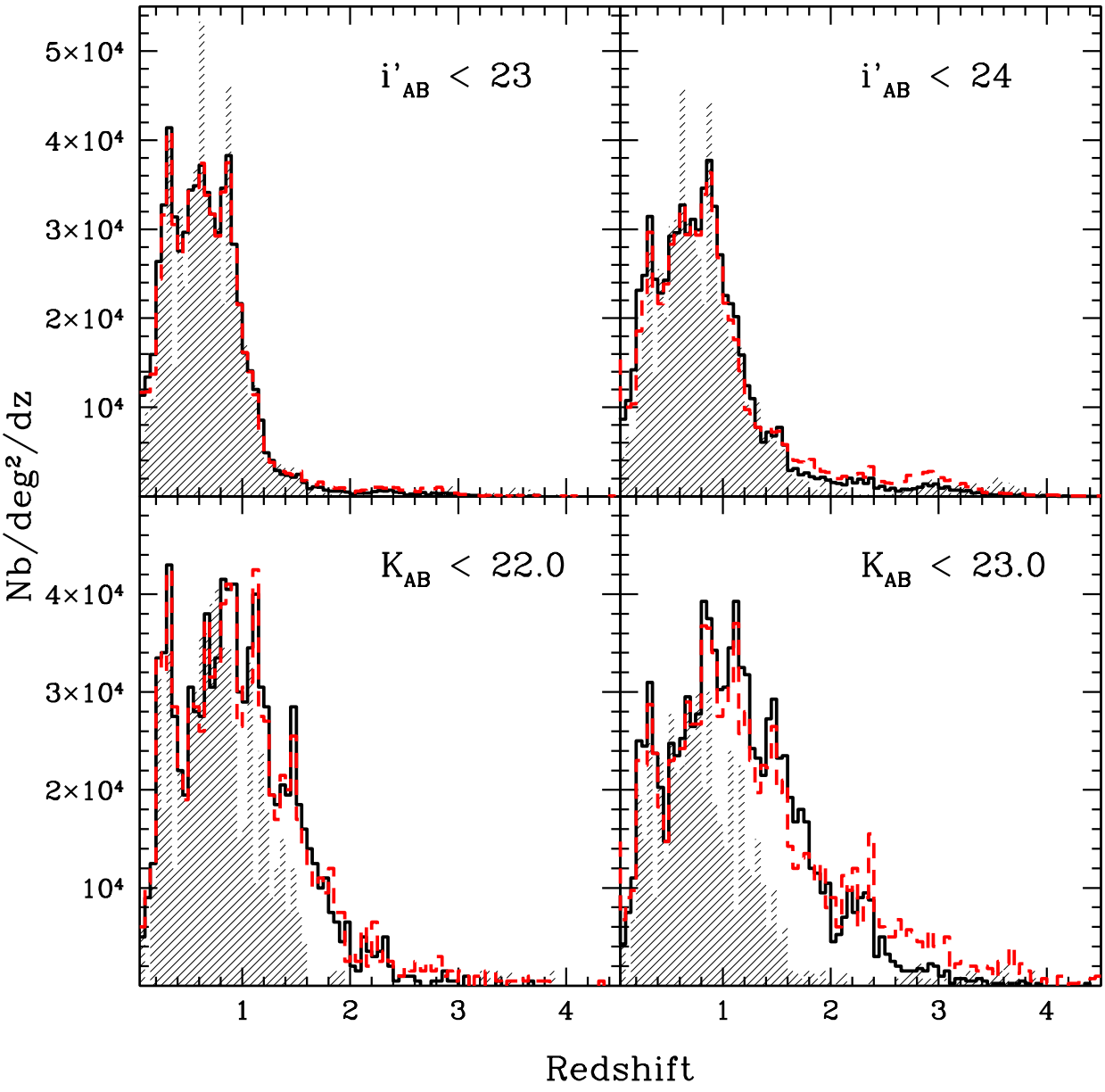

Fig. 12. Comparison between the photometric redshift distributions and the VVDS spectroscopic redshift distributions on the CFHTLS-D1 field, for samples selected at $i'_{AB} < 23$ (top left), $i'_{AB} < 24$ (top right), $K_{AB} < 22$ (bottom left) and $K_{AB} < 23$ (bottom right). The black solid lines and the red dashed lines correspond respectively to the estimate with and without using the prior on the redshift distribution. These distributions are compared with the spectroscopic redshift distributions (shaded histograms) from the VVDS sample, originally selected at $I_{AB} \leq 24$. To maintain the same vertical axis, the redshifts distributions are divided by a factor of two for $i' \leq 24$, $K \leq 23$.

Magnitude cut	$i^* \leq 23$	$i^* \leq 24$	$Ks \leq 22$	$Ks \leq 23$
z_m	0.76	0.90	0.90	1.07
% at $z > 1$	13%	28%	28%	43%

Table 3. Median redshifts and fraction of galaxies at $z > 1$ for samples selected according to $i'_{AB} \leq 23, 24$ and $K_{AB} \leq 22, 23$ in the CFHTLS-D1

	D1	D2	D3	D4
$17.5 < i'_{AB} < 22$	0.49	0.48	0.49	0.48
$22 < i'_{AB} < 23$	0.75	0.75	0.75	0.81
$23 < i'_{AB} < 24$	0.89	0.86	0.86	0.95
$24 < i'_{AB} < 25$	1.00	0.95	0.94	1.03

Table 4. Median redshifts in the four CFHTLS deep fields (columns) for samples selected according to $17.5 < i'_{AB} < 22$, $22 < i'_{AB} < 23$, $23 < i'_{AB} < 24$, $24 < i'_{AB} < 25$ from the top to the bottom, respectively.

most reliable photometric redshifts on this sub-sample with $\eta = 2.1\%$ and $\sigma_{|\Delta z|/(1+zs)} = 0.035$.

We present in Figure 12 the redshift distributions for samples selected with $K_{AB} \leq 22$ and 23. Comparing the photometric and spectroscopic redshift distributions, we see a large difference in the high redshift tail which is explained by the colour incompleteness caused by the $I_{AB} \leq 24$ selection function of the spectroscopic sample. The median redshifts and the fraction of galaxies with $z > 1$ are given in Table 3. As expected, we find that near-infrared selected samples are more efficient to target a high redshift population than i' selected sample. We find 43% of the galaxies at $z > 1$ for a sample selected at $K_{AB} \leq 23$. As previous K selected surveys (Cimatti et al. 2002, Somerville et al. 2004) have found, a large population of galaxies at $z > 1$ is observed.

7. Photometric redshifts in the CFHTLS "Deep Fields" D1, D2, D3 and D4

We finally use the photometric redshift calibration derived from the CFHTLS-D1 field and the VVDS spectroscopic sample to derive photometric redshifts for all fields of the CFHTLS deep survey.

The three CFHTLS deep fields D2, D3, D4 have been imaged with the same instrument and are reduced homogeneously in exactly the same way as the D1 field (McCracken et al. 2006, in preparation). We therefore assume that we can measure the photometric redshifts for these fields in the same manner as we have for the D1 field. As a consistency check, we use 364 spectroscopic redshifts from the DEEP1 survey (Phillips et al. 1997) which are in the D3 field. This allows us to test blindly the quality of these photometric redshifts without any additional calibration. The comparison is shown in the bottom panel of Figure 14. We find $\eta = 3.8\%$ and $\sigma_{|\Delta z|/(1+zs)} = 0.035$ at $i'_{AB} \leq 24$ and $z < 1.5$, without any systematic trend. We therefore conclude that our calibration method derived from D1 can be applied to the other CFHTLS deep fields.

The photometric redshift quality using only the u^*, g', r', i', z' has already been discussed in Section 6.3, but only for the CFHTLS-D1 field and for $i'_{AB} \leq 24$. Since we have already demonstrated in Section 5.3 that the 1σ error bars are representative of a measurement at 68% of confidence level, we use the 1σ error bars to quantify the accuracy of the photometric redshifts in the different fields and beyond the spectroscopic limit. Figure 15 shows the fraction of photometric redshifts with a 1σ error bar left than $0.15 \times (1 + z)$. The best constraint is obtained on the CFHTLS-D1 field and gradually declines for the D4, D3 and D2. The constraint on the photometric redshifts is the lowest on the D2, which is expected since the total exposure times in the u^* and z' bands are respectively 7.7 and 1.7 times lower for the D2 field than for the the D1 field. We note that the specific trends described in Section 6.1 and shown in Figure 13 could partially affect the photometric redshift estimates for the CFHTLS-D2 given than this field has substantially shallower u^* and z' data. The other significant trends observed in Figure 15 are expected from our previous comparisons:

- the redshift range $0.2 < z \leq 1.5$ is the most suitable for the 4 fields which is expected since this redshift range is constrained by the set of filters used.
- the accuracy of the photometric redshifts decreases toward fainter apparent magnitudes, faster at $i'_{AB} > 24$. For $0.2 < z < 1.5$, the fraction of galaxies with $\sigma_{zp}(68\%) > 0.15 \times (1+z)$ remains greater than $\sim 80\%$ at $i'_{AB} = 25$ in the CFHTLS-D1 field.

We show in Figure 16 the redshift distributions for the four CFHTLS deep fields. As expected, the median redshift increases for fainter samples (Table 4) rising from $z_m \sim 0.45$ at $i'_{AB} \leq 22$ to $z \sim 1$ at $24 \leq i'_{AB} \leq 25$. The median redshifts are in good agreement between the four fields. The redshift distribution in the D4 is shifted at higher redshift. We observe significant variations of the redshift distribution between the four fields. Figure 17 shows the ratio between the redshift distribution in each field and the redshift distribution averaged over the four fields, using a redshift step of $\Delta z = 0.1$. This ratio shows that the difference in redshift distribution can reach at most a factor 1.6 in a redshift bin $\Delta = 0.1$ (at z=0.25 between the D2 and the D4 fields). The average dispersion in the interval $0.2 < z < 1.5$ and in a redshift slice $\Delta = 0.1$ is $\sim 15\%$. We conclude that the cosmic variance can be important for fields of $\sim$0.8 deg^2. We note however that the four fields do not reach exactly same depth in all filters which could be responsible for some of the differences between the redshifts distributions.

8. Conclusions

Using the unique combination of the deep $u^*g'r'i'z'$ multiband imaging data from the CFHTLS survey supplemented by shallower $BVRI$ data from the VVDS imaging survey (and also by J and K data on a smaller sub-area) and VVDS first epoch spectroscopic redshifts, we have been able to obtain very accurate photometric redshifts on the CFHTLS-D1 field. We reach $\sigma_{\Delta z/(1+z)} = 0.037$ at $i' \leq 24$ and $\eta = 3.7\%$ of catastrophic errors (defined strictly as $\Delta z > 0.15(1 + z)$). For the bright sample selected at $i_{AB} \leq 22.5$, we reach $\sigma_{\Delta z/(1+z)} = 0.030$ and $\eta = 1.7\%$.

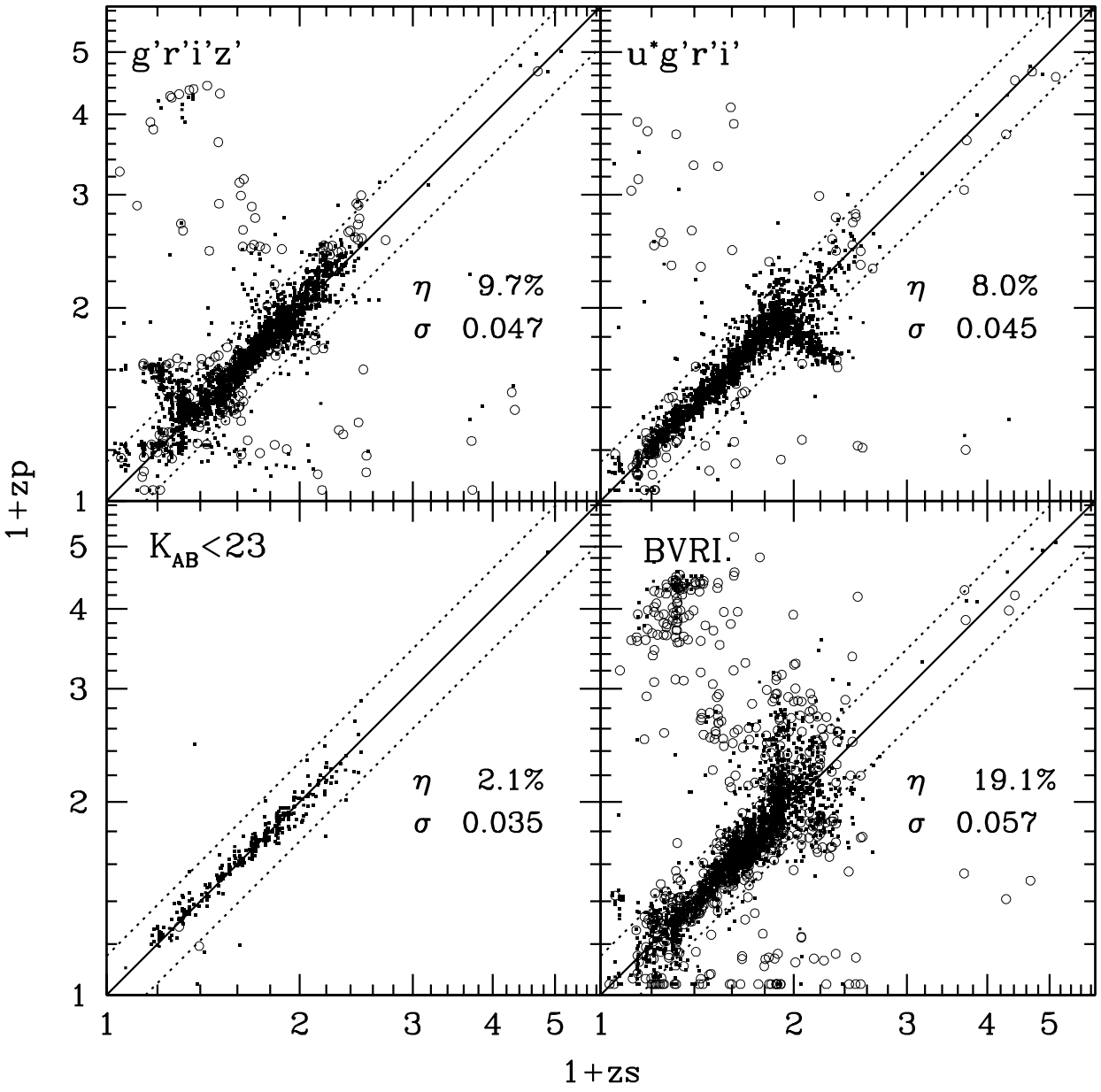

Fig. 13. Comparison between spectroscopic and photometric redshifts for different combinations of filters. The photometric redshifts in the top left and right panel are computed without using the deep u^*/z' band respectively. The bottom left panel shows the photometric redshifts for a near-infrared selected sample computed using B, V, R, I, u^*, g', r', i, z', J and K bands. The bottom right panel shows the photometric redshifts obtained using the B, V, R, I bands from the VVDS survey.

This accuracy has been achieved by calibrating our photometric redshifts using a large and deep spectroscopic sample of 2867 galaxies. We have established a reliable calibration method combining an iterative correction of photometric zero-points, template optimisation, and a Bayesian approach. This method removes some obvious systematic trends in the estimate and reduces by a factor 2.3 the fraction of catastrophic errors.

We have investigated in detail the quality of photometric redshifts as a function of spectral type, apparent magnitude and redshift based on the comparison with the VVDS spectroscopic redshifts. This step is crucial for forthcoming scientific analysis. As expected we find that the apparent magnitude is the key parameter: the fraction of catastrophic errors increases by a factor 12 and the rms by a factor 1.7 between $17.5 \leq i'_{AB} \leq 21.5$ and $23.5 \leq i'_{AB} \leq 24$. The reliability of the photometric redshifts also depends on the spectral type: half of the catastrophic errors are galaxies which are best fitted by a starburst template type. The evolution of η as a function of

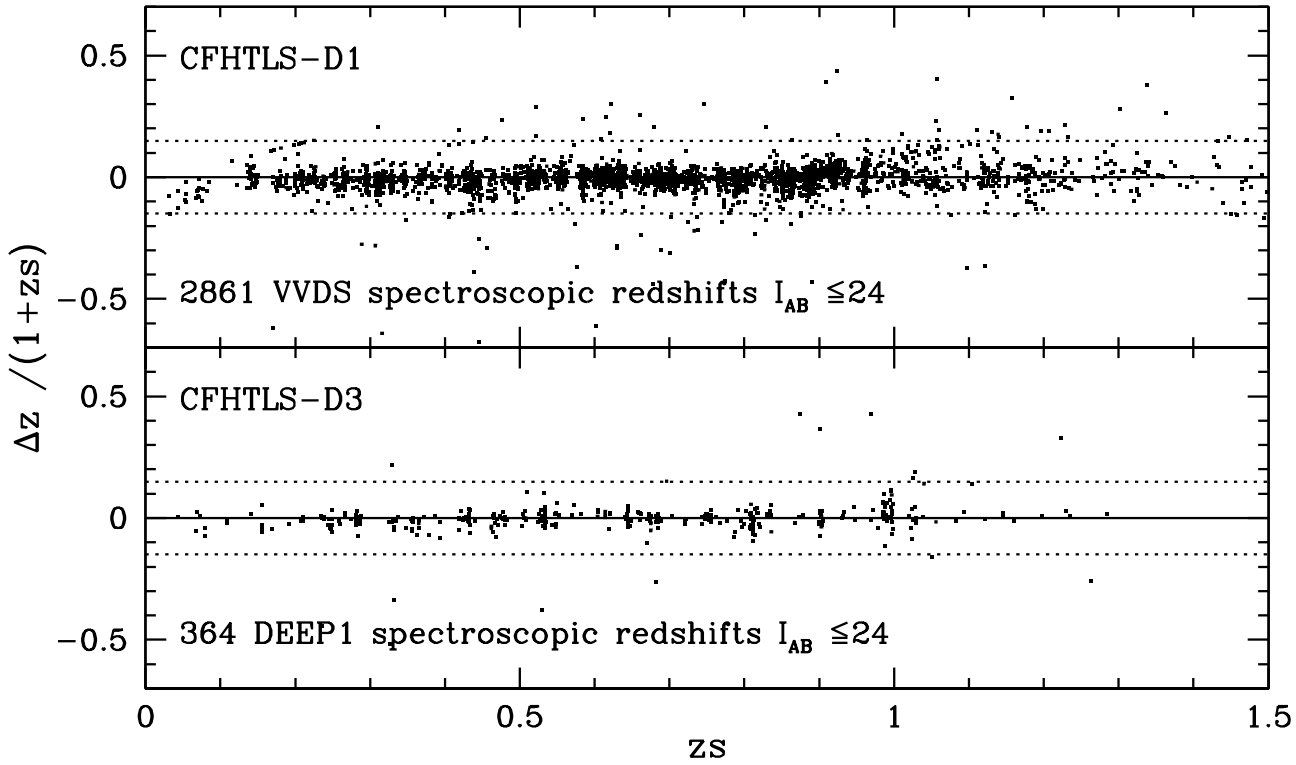

Fig. 14. Δz as a function of redshift. The photometric redshifts are computed using the CFHTLS filter set u^*, g', r', i', z'. The top and bottom panels present the photometric redshifts obtained on the CFHTLS-D1 and CFHTLS-D3 fields respectively.

redshift shows that the redshift range the most reliable for forthcoming scientific analysis is $0.2 < zp < 1.5$ for the complete population of galaxies. This range can be extended into the "redshift desert" when near-infrared data are available (although currently only 6% of the field is covered).

We present i' band selected redshift distributions at $i'_{AB} \leq 23$ and $i'_{AB} \leq 24$ which are fully consistent with the redshift distributions derived from the VVDS spectroscopic redshifts. We show the ability of our method to correctly recover the redshift distributions, including even the identification of the strongest density peaks. We show that a near-infrared selected sample is very efficient for the selection of high redshift galaxies, with 40% of the sample at $z > 1$ for $K \leq 23$. This robust K selected sample will be used to investigate the evolution of the stellar mass function (Pozzetti et al. 2006, in preparation) which is a crucial test of the hierarchical model (e.g. Kauffmann & Charlot 1998, Cimatti et al. 2002, Somerville et al. 2004) of galaxy formation.

Finally, we have applied our robust photometric redshifts measurement code on all four CFHTLS deep fields (*http://www.cfht.hawaii.edu/Science/CFHTLS*). We measure photometric redshifts for an uniquely large and deep sample of 522286 objects at $i'_{AB} \leq 25$ on 3.2 deg^2. We assess the accuracy of these photometric redshifts beyond the spectroscopic limits and we present the redshift distributions in these four deep fields showing that cosmic variance effects are present at the 15% level for fields of size 0.8 deg^2.

All photometric redshifts and input photometric catalogues are made publicly available.

Acknowledgements. This research has been developed within the framework of the VVDS consortium. This work has been partially supported by the CNRS-INSU and its Programme National de Cosmologie (France) and Programme National Galaxies (France), and by Italian Ministry (MIUR) grants COFIN2000 (MM02037133) and COFIN2003 (num.2003020150). The VLT-VIMOS observations have been carried out on guaranteed time (GTO) allocated by the European Southern Observatory (ESO) to the VIRMOS consortium, under a contractual agreement between the Centre National de la Recherche Scientifique of France, heading a consortium of French and Italian institutes, and ESO, to design, manufacture and test the VIMOS instrument.

References

Arnouts S., Cristiani S., Moscardini L. et al., 1999, MNRAS, 310, 540
Arnouts S., Moscardini L., Vanzella E. et al., 2002, MNRAS, 329, 355
Baum W. A., 1962, IAU Symp., 15, 390
Benítez N., 2000, ApJ, 536, 571
Benítez N., Ford H., Bouwens R. et al., 2004, ApJS, 150, 1
Bertin E. & Arnouts S., 1996, A&AS, 117, 393
Bolzonella M., Miralles J.-M. & Pelló R., 2000, A&A, 363, 476
Bolzonella M., Pelló R., & Maccagni D., 2002, A&A, 395, 443

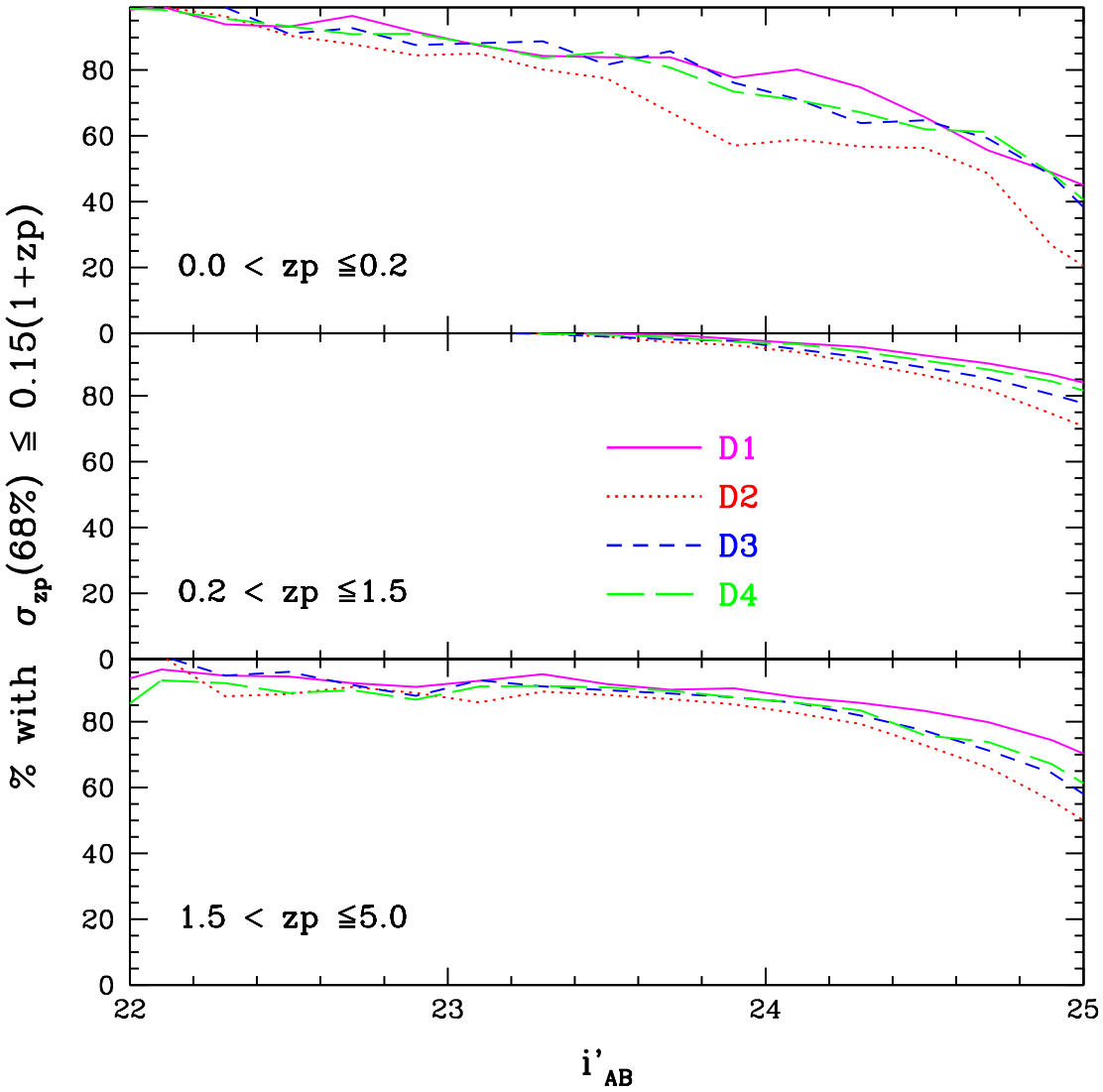

Fig. 15. Fraction of photometric redshifts with an error bar 68% smaller than $0.15 \times (1 + zp)$ as a function of i' apparent magnitude. This statistic is shown in the four CFHTLS deep fields: D1 (solid line), D2 (dotted line), D3 (short dashed line) and D3 (long dashed line) and in the three redshift ranges $0 < z \leq 0.2$ (top panel), $0.2 < z \leq 1.5$ (middle panel) and $1.5 < z \leq 5$ (bottom panel).

Brodwin M., Lilly S.J., Porciani C. et al., 2006, ApJS, 162, 20
Boulade O., Charlot X., Abbon P. et al., 2003, SPIE, 4841, 72
Bruzual G. et Charlot S., 2003, MNRAS, 344, 1000
Budavári T., Szalay A. S., Connolly A. J., Csabai I. & Dickinson M., 2000, AJ, 120, 1588
Coleman G.D., Wu C.-C., Weedman D.W., 1980, ApJS, 43, 393
Connolly A. J., Csabai I., Szalay A. S., Koo D. C., Kron R. G., & Munn J. A., 1995, AJ, 110, 2655
Csabai I., Connolly A. J., Szalay A. S. & Budavári T., 2000, AJ, 119, 69
Cimatti A., Pozzetti L., Mignoli M. et al., 2002, A&A, 391, L1
Fernández-Soto A., Lanzetta K. M. & Yahil A., 1999, ApJ, 513, 34
Fioc M. & Rocca-Volmerange B., 1997, A&A, 326, 950
Fontana A., D'Odorico S., Poli F. et al., 2000, AJ, 120, 2206
Gabasch A., Bender R., Seitzer S. al., 2004, A&A, 421, 41
Ilbert O., Tresse L., Zucca E. et al., 2005, A&A, 439, 863
Iovino A., McCracken H.J., Garilli B. et al., 2005, A&A, in press, astro-ph/0507668
James F. & Roos M., 1995, MINUIT Function Minimization and Error Analysis, Version 95.03, CERN Program Library D506
Kauffmann G. & Charlot S., 1998, MNRAS, 297, L23
Kinney A.L., Calzetti D., Bohlin R.C., McQuade K., Storchi-Bergmann T. & Schmitt H.R., 1996, ApJ, 467, 38
Kron R.G., 1980, ApJS, 43, 305
Le Fèvre O., Saisse M., Mancini D. et al., 2003, SPIE, 4841, 1670
Le Fèvre O., Mellier Y., McCracken H. J. et al., 2004a, A&A, 417, 839
Le Fèvre O., Vettolani G., Paltani S. et al., 2004b, A&A, 428, 1043
Le Fèvre O., Vettolani G., Garilli B. et al., 2005a, A&A, 439, 845

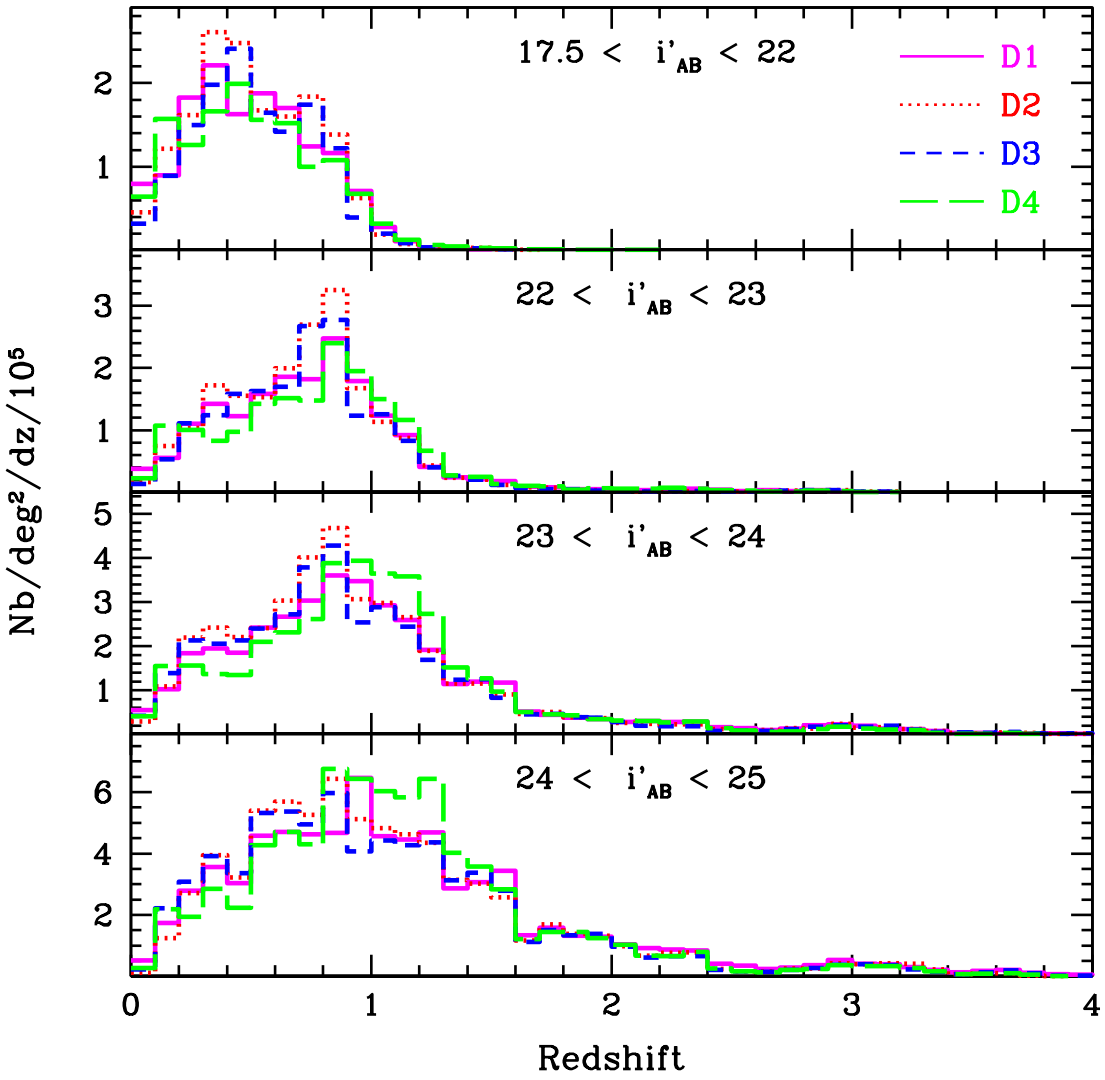

Fig. 16. Photometric redshift distributions in the 4 fields CFHTLS-D1 (solid line), CFHTLS-D2 (dotted line), CFHTLS-D3 (short dashed line) and CFHTLS-D4 (long dashed line). The redshift distribution are shown from bright ($17.5 < i'_{AB} < 22$) to faint selected samples ($24 < i'_{AB} < 25$) from the top to the bottom, respectively.

Le Fèvre O., Paltani P., Arnouts S. et al., 2005b, nature, 437, 519
Madau P., 1995, ApJ, 441, 18
McCracken H.J., Radovich M., Bertin E. et al., 2003, A&A, 410, 17
McCracken H. J. et al., 2006, A&A, in preparation
Mobasher B., Idzi R., Bentez N. et al., 2004, ApJL, 600, L167
Pickles A. J., 1998, PASP, 110, 863
Phillips A.C., Andrew C., Guzman R. et al., 1997, ApJ, 489, 543
Pozzetti L. et al., 2006, A&A, in preparation
Prevot M.L., Lequeux J., Prevot L., Maurice E. & Rocca-Volmerange B., 1984, A&A, 132, 389
Puschell J.J., Owen F.N. & Laing R.A., 1982, ApJL, 257, L57
Sawicki M.J., Lin H. & Yee H.K.C., 1997, AJ, 113, 1
Schlegel D. J., Finkbeiner D. P., & Davis M., 1998, ApJ, 500, 525
Somerville R.S., Moustakas L.A., Mobasher B. et al., 2004, ApJL, 600, L135
Vanzella E., Cristiani S., Fontana A. et al., 2004, A&A, 423, 761
Wang Y., Bahcall N. & Turner E.L., 1998, AJ, 116, 2081
Wolf C., Meisenheimer K., Rix H.-W. et al., 2003, A&A, 401, 73
Wolf C., Meisenheimer K., Kleinheinrich M. et al., 2004, A&A, 421, 913

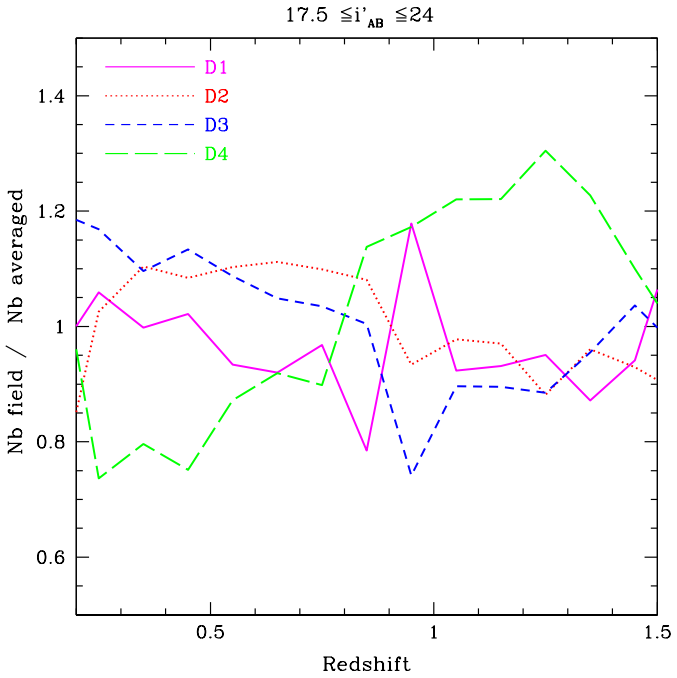

Fig. 17. Ratio between the redshift distributions in each field and the redshift distribution averaged over the 4 fields. Symbols for each field are the same than Figure 16.